Electromechanical Energy Conversion Systems (EECS),
Niroo Research Institute.
Vol. 1, Issue. 2. Spring 2021

High-Frequency Physics-Based Analytical Modeling of Permanent Magnet Synchronous Motor

Alireza Rahimi *, Khalil Kanzi

Iranian Research Institute for Electrical Engineering (IREE), ACECR, Tehran, Iran

Department of Electrical Engineering, ACECR, Tehran, Iran

**Corresponding author, Email: alirezarahimi1@gmail.com, khkanzi@gmail.com*

Abstract

In this paper, a physics-based analytical method is proposed in order to model the frequency behavior of laminated iron-core permanent magnet synchronous motor (PMSM). The proposed model consists of frequency-dependent lumped circuit parameters representing two parts; Iron-core and stator winding. These frequency-dependent components represent the skin effect and proximity effect in conductors and eddy-currents effect in the core. The total parasitic capacitance is considered to be frequency-independent and estimated from measured impedance characteristics of the PMSM. In order to verify the accuracy of the proposed model, we compared the equivalent AC resistance and AC inductance of one phase of a counter-rotating PMSM calculated from the proposed analytical method with the 3D finite element analysis (FEA) results. Finally, the Impedance characteristic of the test PMSM calculated using the proposed method is verified by the impedance measurement data, which shows a good agreement. The method proposed in this paper can be used for modeling various high-frequency issues in variable speed drives (VSDs) such as electromagnetic interference (EMI), common-mode bearing currents, and long-cable effects on motor terminals.

Keywords: High-frequency PMSM modeling; laminated iron magnetic cores; physics-based modeling; Analytical modeling; eddy-currents effect;

1. INTRODUCTION

Increasing the switching frequency in variable speed drive (VSD) systems is advantageous because it reduces current and torque ripples. However, it leads to circulating bearing currents through the frame and shaft of the motor, which flows in common-mode (CM) and differential-mode (DM) paths, causing conducted electromagnetic interference (EMI) [1-5]. Literature has been investigating various methods for modeling, measuring, and attenuating this issue in the last few decades [1-13]. Accurate modeling of the high-frequency behavior of a VSD system requires a detailed high-frequency model of its different parts. Electrical motors play a significant role at high-frequencies providing conducted paths for CM and DM current flow in a drive system through parasitic capacitances [14, 15]. Hence, it is crucial to have a detailed model of the motor, which represents the high-frequency behavior of the motor with high accuracy at the desired frequency range.

Iron-core of the motor behaves differently under the influence of a high-frequency excitation in comparison with the case of power-frequency excitation. At high frequencies, the iron-core acts as a barrier for the magnetic flux due to the eddy-currents effect and Lenz's law. Therefore, the self and mutual inductances of the winding are frequency-dependent parameters. Moreover, due to skin and proximity effects, the resistance of the winding also increases with frequency.

Generally, high-frequency motor modeling studies in literature can be classified into two types: distributed parameter models and lumped parameter models. Distributed parameter models consider attributes such as resistance, inductance, and capacitance distributed continuously throughout the winding. On the other

hand, the lumped parameter models consider all attributes into ideal electrical components. Even though distributed parameter models are more accurate than lumped parameter models, lumped parameter models are more prevalent at high-frequency modeling due to their acceptable accuracy and the simple structure. However, different authors used both models in the last few decades.

Physics-based parameters estimation requires the design properties of the motor, e.g., geometry, material properties, and windings configuration. Using analytical calculations or numerical methods such as finite element analysis (FEA), parasitic parameters of the model can be extracted [16-20]. On the other hand, in behavioral parameters estimation, parasitic parameters of the motor are obtained from impedance characteristics of the motor using various fitting methods [11, 21, 22].

In this paper, a physics-based analytical method is developed for estimating frequency-dependent lumped circuit parameters in order to model the permanent magnet synchronous motor (PMSM) impedance behavior at high-frequencies. Physics-based modeling by numerical methods requires a complex simulation set-up with additional software for 3D FEA analysis. Parameters estimation using physics-based modeling needs more effort, as well as longer simulation times, compared to behavioral modeling. However, the proposed method in this paper is based on the design parameters of PMSM using analytical equations. Analytical modeling is much faster than 3D FEA, and it gives a good understanding of how different parts of the motor's design and properties affect its frequency behavior.

In section II-A, the iron-core model is developed analytically based on the high-frequency model of laminated inductor presented in [23]. The model is using electromagnetic field analysis, taking into account eddy-currents in the iron-core. The magnetic permeability and electrical conductivity of iron are assumed to be independent of frequency.

In section II-B, stator windings are modeled by analytical formulation, taking into account proximity and skin effects in the conductors. The stator leakage inductance is modeled as the sum of different leakage inductances. Due to the randomness of conductors in the stator slots, calculating accurate parasitic capacitances using a physics-based modeling method is not possible [3, 4]. It is much convenient to estimate the parasitic capacitances from the impedance characteristics of the motor. The total equivalent parasitic capacitance of stator winding is assumed to be independent of frequency and estimated from impedance characteristics. Finally, a PMSM is modeled using the proposed method, and the results are verified with 3D FEA simulation results and experimental measurement of motor phase impedance characteristics.

2. High-Frequency Motor Model

Fig. 1(a) shows the lumped parameters RLC equivalent circuit of one phase of a PMSM. Where R_{ac} and L_{ac} are respectively, equivalent AC resistance and equivalent AC inductance of the motor, and both are frequency-dependent components. In order to determine the model parameters as functions of frequency, analytical models for both laminated iron-core and winding are developed respectively in Sections II-A and II-B. The total parasitic capacitance of each phase C is considered frequency independent and modeled in section II-B by using the measured winding impedance characteristic.

Fig. 1(b) shows the equivalent series circuit of the proposed model, which used by most impedance meters. In section II-B, equivalent series parameters are determined in order to compare the modeling results with the measurements obtained from the LCR meter.

A. Iron-Core Model

A lamination packet of PMSM consists of the stator and rotor core, stator winding conductors and air-gap in an axial cross-section of the motor without the surface-mounted magnets is shown in Fig. 2. From the top view, as shown in Fig. 3, R_{so} is the outer radius, and R_{si} is the inner radius of the stator, R_{ro} is the outer radius, and R_{ri} is the inner radius of the rotor. The stator slots are neglected in the model. Therefore, winding currents are distributed from R_1 to R_2 around the air-gap and flow in the direction of the z-axis.

Consider two arbitrary orthogonal paths, one in the r-θ plane (I) and one in the r-z plane (II), as shown in Fig. 2. Each of the paths has a core part and an air-gap part. From Ampère's circuital law we have:

$$F_{12} + F_{23} + F_{34} + F_{41} = \iint_I J_z \, ds \tag{1}$$

$$F_{34} + F_{45} + F_{56} + F_{63} = \iint_{II} J_\theta \, ds \tag{2}$$

where F is the MMF along the path, and J_z is the current density flows in the stator windings along the z-axis.

It is assumed that the winding is carrying current in the z-direction, and this current is uniform in the radial dimension. Considering a single phase of the armature is carrying current, the fundamental component of current density will be:

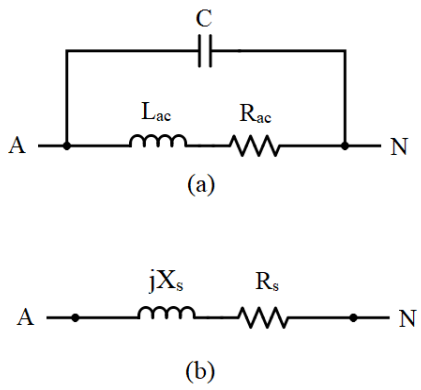

Fig. 1. Proposed lumped parameter circuit model. (a) RLC equivalent circuit (b) Series equivalent circuit

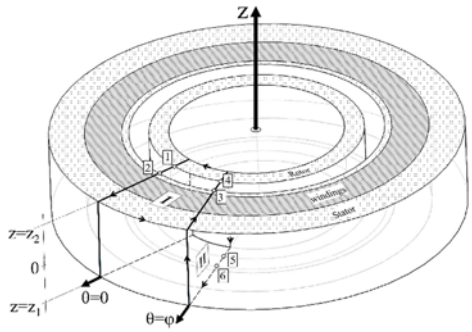

Fig. 2. A lamination packet of an AC motor core and windings (without surface-mounted magnets)

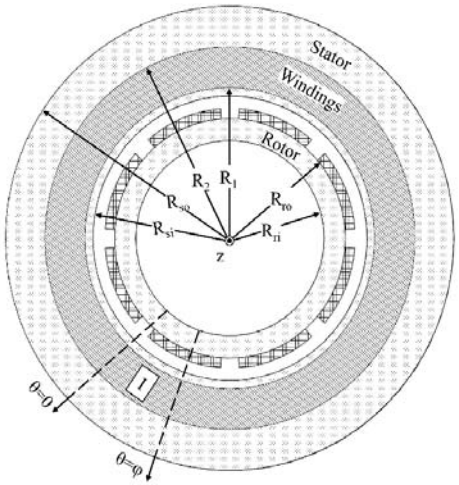

Fig. 3. Top view of a cross-section of an AC motor

$$J_{z1} = \frac{4}{\pi}\frac{N_a I_a}{R_2^2 - R_1^2} K_{w1} \tag{3}$$

where K_{w1} the 1st harmonic winding factor is:

$$K_{w1} = \frac{\sin\frac{\theta_{\omega e}}{2}}{\frac{\theta_{\omega e}}{2}} \tag{4}$$

Moreover, $\theta_{\omega e}$ is the electrical winding angle which for a p pole pair motor is:

$$\theta_{\omega e} = p\theta_{\omega} \tag{5}$$

The magnetic field intensity vector H_r in the core has only the r-component, which depends on the coordinate along the thickness and time only. Similarly, the eddy-current density vector J_θ has the θ-directed component only. Considering H only has r axis component, the MMF's along the paths orthogonal to r axis is zero. Then by subtracting (1) from (2), we have:

$$\begin{aligned}
&\int_{R_{so}}^{R_{si}} H_{cr}(0,z_2,t)dz + \int_{R_{si}}^{R_{ro}} H_{gr}(0,z_2,t)dz \\
&+\int_{R_{ro}}^{R_{ri}} H_{cr}(\varphi,z_2,t)dz + \int_{R_{so}}^{R_{si}} H_{cr}(0,z_1,t)dz \\
&+\int_{R_{si}}^{R_{ro}} H_{cr}(0,z_1,t)dz + \int_{R_{ro}}^{R_{ri}} H_{cr}(\varphi,z_1,t)dz \\
&= \int_{R_1}^{R_2}\int_0^{\varphi} \frac{4}{\pi}\frac{N_a I_a(t)}{R_2^2 - R_1^2} K_{w1} r d\theta dr + \int_{z_1}^{z_2}\int_{R_{ri}}^{R_{so}} J_\theta(z,t)\mathrm{d}r dz
\end{aligned} \tag{6}$$

where $H_r(\varphi,z,t)$ is the magnetic flux intensity. Neglecting fringing effects in the air-gap and taking into account the continuity of the magnetic flux density at the boundary between the air-gap and iron-core, it follows that:

$$\begin{aligned}
&B_{cr} = B_{gr} \\
&\mu_0 H_{gr} = \mu_c H_{cr} \Rightarrow H_{gr} = \mu_{cr} H_{cr}
\end{aligned} \tag{7}$$

where $\mu_c = \mu_0\mu_{cr}$ is the absolute magnetic permeability, and μ_{cr} is the relative magnetic permeability of the laminated sheet. Substituting (7) in (6) we have:

$$\begin{aligned}
&(R_{ro} - R_{ri})H_{cr}(0,z_2,t) + \mu_{cr}(R_{si} - R_{ro})H_{cr}(0,z_2,t) \\
&+(R_{so} - R_{si})H_{cr}(0,z_2,t) \; + \; (R_{so} - R_{si})H_{cr}(\varphi,z_1,t) \\
&+\mu_{cr}(R_{si} - R_{ro})H_{cr}(\varphi,z_1,t) + (R_{ro} - R_{ri})H_{cr}(\varphi,z_1,t) \\
&= \int_{R_1}^{R_2}\int_0^{\varphi} \frac{4}{\pi}\frac{N_a I_a(t)}{R_2^2 - R_1^2} K_{w1} r d\theta dr + \int_{z_1}^{z_2}\int_{R_{ri}}^{R_{so}} J_\theta(z,t)\mathrm{d}r dz
\end{aligned} \tag{8}$$

Since the total eddy-currents in any sheet is zero, the magnetic field intensity in the considered sheet is not influenced by the remaining sheets and, because the symmetry of one pole $z_2=-z_1=z$ and $\varphi=\pi/p=\varphi_p$ we have:

$$H_{cr}(0,z,t) = H_{cr}(\varphi_p,-z,t) = H_r(z,t) \tag{9}$$

Substituting (9) in (8) we have:

$$H_r(z,t)(l_c) = \frac{\mu_e}{\mu_c} N_a \left[\int_{R_1}^{R_2} \int_0^{\varphi} \frac{4}{\pi} \frac{I_a(t) K_{w1}}{R_2^2 - R_1^2} r d\theta dr + \frac{l_c}{N_a} \int_{-\frac{s}{2}<z<\frac{s}{2}}^{s/2} J_\theta(z,t) dr dz \right] \quad (10)$$

where l_c is the path length in the iron-core and μ_e is the effective magnetic permeability:

$$\mu_e = \mu_c \frac{l_c / 2}{l_c + \mu_{rc} \delta_{ef}} \quad (11)$$

where δ_{ef} is the effective air-gap length.

From (10), we can write

$$\frac{\partial H_r(z,t)}{\partial z} = \frac{\mu_e}{\mu_c} \frac{\partial}{\partial z} \left[\int_z^{s/2} J_\theta(z,t) dz \right] = -\frac{\mu_e}{\mu_c} J_\theta(z,t) \quad (12)$$

Applying Ohm's law and Faraday's law, we have:

$$\frac{\partial H_r(z,t)}{\partial z} = -\frac{\mu_e}{\rho_c \mu_c} \frac{\partial E_\theta(z,t)}{\partial z} = \frac{\mu_e}{\rho_c} \frac{\partial H_r(z,t)}{\partial t} \quad (13)$$

Introducing the magnetic field intensity phasor $\hat{H}_r(z)$ for the sinusoidal steady-state at angular frequency ω. We can write:

$$\frac{d^2 \hat{H}_r(z)}{dz^2} = \hat{k}_t^2 \hat{H}_r(z) \quad (14)$$

where

$$\hat{k}_t = \sqrt{\frac{j\omega\mu_e}{\rho_c}} = \frac{1+j}{\delta_t} \quad (15)$$

and

$$\delta_t = \sqrt{\frac{\rho_c}{\pi \mu_e f}} \quad (16)$$

The differential equation (14) has a general solution given by:

$$\hat{H}_r(z) = \hat{A} e^{\hat{k}_t} + \hat{B} e^{-\hat{k}_t} \quad (17)$$

From (9) we have:

$$\hat{H}_r(z) = \hat{H}_r(-z) \quad (18)$$

Equation (18) can then be written in the form:

$$\hat{H}_r(z) = \hat{C} \cosh \hat{k}_t z \quad (19)$$

Applying the boundary conditions to (19) yields:

$$\hat{H}_r(z) = \hat{H}_{ro} \frac{\cosh\left(\frac{1+j}{\delta_t} z\right)}{\cosh\left(\frac{1+j}{\delta_t} \frac{s}{2}\right)} \quad (20)$$

where $\hat{H}_{ro}$ is the magnetic field intensity phasor at the boundary of the sheet, i.e., for $z=\pm s/2$. In order to determine $\hat{H}_{ro}$, the eddy-current density phasor $\hat{J}_\theta(z)$ in any sheet can be calculated using the differential form of the Maxwell-Faraday law. Neglecting the displacement current density in iron, which is much lower than the conduction current density:

$$\hat{J}_\theta = \left(\nabla \times \hat{H}_r(z)\right)_\theta = -\hat{H}_{ro} \left(\frac{1+j}{\delta_t}\right) \frac{\sinh\left(\frac{1+j}{\delta_t} z\right)}{\cosh\left(\frac{1+j}{\delta_t} \frac{s}{2}\right)} \quad (21)$$

From (21), it follows that the phasor $\hat{J}_\theta(z)$ is an odd function of z:

$$\hat{J}_\theta(z) = -\hat{J}_\theta(-z) \quad (22)$$

Hence, (10) written for $z=\pm s/2$ and in terms of phasor gives:

$$\hat{H}_{ro} = \frac{\mu_e}{l_c \mu_c} \int_{R_1}^{R_2} \int_0^{\varphi_p} \frac{4}{\pi} \frac{N_a \hat{I}_a}{R_2^2 - R_1^2} K_{w1} r d\theta dr = \frac{\mu_e}{\mu_c} \frac{2 K_{w1} N_a}{l_c p} \hat{I}_a \quad (23)$$

where $\hat{I}_a$ is the phasor of the sinusoidal current flowing through the phase winding. From (7) the air-gap flux density $B_{gr}(z)$ is:

$$\hat{B}_{gr}(z) = \mu_c \hat{H}_r(z) = \mu_c \hat{H}_{ro} \frac{\cosh\left(\frac{1+j}{\delta_t} z\right)}{\cosh\left(\frac{1+j}{\delta_t} \frac{s}{2}\right)} \quad (24)$$

Thus, the air-gap magnetic flux phasor Φ_s throughout a cross-section of any sheet over one pole surface S_p is:

$$\hat{\Phi}_s = \iint_{S_p} \hat{B}_{gr}(z) ds = 2 \int_0^{s/2} \int_0^{\varphi_p} \mu_c \hat{H}_{ro} \frac{\cosh\left(\frac{1+j}{\delta_t} z\right)}{\cosh\left(\frac{1+j}{\delta_t} \frac{s}{2}\right)} r d\theta dz$$
$$= 2 \mu_c \tau_p \left(\frac{\delta_t}{1+j}\right) \tanh\left(\frac{1+j}{\delta_t} \frac{s}{2}\right) \hat{H}_{ro} \quad (25)$$

where τ_p is the pole pitch. Neglecting the leakage flux through the thin gaps between adjacent sheets, the magnetic flux linking one phase winding is:

$$\hat{\lambda}_a = K_{w1} N_a \hat{\Phi}_s = \frac{2 s \mu_e \tau_p (K_{w1} N_a)^2}{\pi p l_c} \left(\frac{\delta_t}{1+j}\right) \tanh\left(\frac{1+j}{\delta_t} \frac{s}{2}\right) \hat{H}_{ro} \quad (26)$$

Substituting (23) into (26) gives

$$\hat{\lambda}_a = L_{m(dc)} \frac{\delta_t}{1+j} \frac{2}{s} \tanh\left(\frac{1+j}{\delta_t} \frac{s}{2}\right) \hat{I}_a \quad (27)$$

where

$$L_{m(dc)} = \frac{2 \mu_e \tau_p s}{\pi l_c p} (K_{w1} N_a)^2 \quad (28)$$

$L_{m(dc)}$ is the DC and low-frequency magnetization inductance. Hence, the voltage induced across the winding by the magnetic flux is:

$$\hat{V}_a = j\omega\hat{\lambda}_a = j\omega L_{m(dc)}\frac{\delta_t}{1+j}\frac{2}{s}\tanh\left(\frac{1+j}{\delta_t}\frac{s}{2}\right)\hat{I}_a \quad (29)$$

Moreover, the impedance of a phase winding is given by

$$\hat{Z}_a = \frac{\hat{V}_a}{\hat{I}_a} = j\omega\hat{\lambda}_a = j\omega L_{m(dc)}\frac{\delta_t}{1+j}\frac{2}{s}\tanh\left(\frac{1+j}{\delta_t}\frac{s}{2}\right) \quad (30)$$

We can write (30) as

$$\hat{Z}_a = \omega L_{m(dc)}\frac{\delta_t}{s}\left(\frac{\sinh\frac{s}{\delta_t}-\sin\frac{s}{\delta_t}}{\cosh\frac{s}{\delta_t}+\cos\frac{s}{\delta_t}}+j\frac{\sinh\frac{s}{\delta_t}+\sin\frac{s}{\delta_t}}{\cosh\frac{s}{\delta_t}+\cos\frac{s}{\delta_t}}\right) \quad (31)$$

The real and imaginary parts of $\hat{Z}_a$ represent the core equivalent parallel resistance R_c (which accounts for the eddy-currents loss in the core) and the coil magnetization reactance $X_m=\omega L_{m(ac)}$, respectively.

$$R_c = \mathrm{Re}(\hat{Z}_a) = \omega L_{m(dc)}\frac{\delta_t}{s}\left(\frac{\sinh\frac{s}{\delta_t}-\sin\frac{s}{\delta_t}}{\cosh\frac{s}{\delta_t}+\cos\frac{s}{\delta_t}}\right) \quad (32)$$

$$L_{m(ac)} = \frac{\mathrm{Im}(\hat{Z}_a)}{\omega} = L_{m(dc)}\frac{\delta_t}{s}\left(\frac{\sinh\frac{s}{\delta_t}+\sin\frac{s}{\delta_t}}{\cosh\frac{s}{\delta_t}+\cos\frac{s}{\delta_t}}\right) \quad (33)$$

B. Stator Winding Model

The winding part of the motor is modeled in three parts. Winding AC resistance, Total leakage inductance, and Total parasitic capacitance.

a) Winding AC Resistance

The resistance of the stator winding R_w can be defined as a multiple of the stator winding DC resistance R_{dc} and AC resistance factor K_R:

$$R_w = K_R R_{dc} \quad (34)$$

R_{dc} depends on the cross-section area and length of the winding conductors. K_R depends on the shape of the conductors and the formation of them in a slot. Detailed calculation of R_{dc} and K_R is available in [24].

The resistance of motor windings increases with frequency because of skin and proximity effects. These effects are due to time-varying electromagnetic fields. The combined result of these two effects reduces the effective cross-sectional area of the wire available for the current flow.

b) Windings Leakage Inductance

Total motor windings leakage inductance can be written as a sum of different leakage inductances. Leakage inductance $L_{l(ac)}$ can be divided into the following partial leakage inductances which can be defined as a multiple of the windings magnetization inductance $L_{m(dc)}$ by a leakage factor:

$$L_{l(ac)} = L_\delta + L_{sq} + L_u + L_d + L_w \quad (35)$$

L_δ is the air-gap leakage inductance, L_{sq} is the skew leakage inductance, L_u is the slot leakage inductance, L_d is the tooth-tip leakage inductance, L_w is the end winding leakage inductance. Detailed calculation of these partial inductances is available in [24]. L_δ, L_{sq}, L_d, and L_w are independent of frequency, but L_u reduces with increasing the frequency.

c) Windings parasitic Capacitances

As mentioned before, because of the randomness of windings and not knowing the actual wire distribution inside the slots, accurate modeling and calculation of the C based on the coil geometry is impracticable. A more convenient way to estimate C is from impedance measurement characteristics of the motor phase.

Fig. 1(a) shows the RLC equivalent circuit of the motor. Fig. 1(b) shows the equivalent series circuit used by most impedance meters. A self-resonant frequency f_r of a motor winding is defined as a frequency at which the reactance X_s becomes zero. Hence, C can be calculated using the measured self-resonant frequency f_r as:

$$C = \frac{1}{(2\pi f_r)^2 L_{ac}(f_r) + \frac{R_{ac}^2(f_r)}{L_{ac}(f_r)}}. \quad (36)$$

where R_{ac} and L_{ac} are the total AC resistance and Inductance shown in Fig. 1(b):

$$R_{ac} = R_w + R_c \quad (37)$$

$$L_{ac} = L_{m(ac)} + L_{l(ac)} \quad (38)$$

The frequency f_r is assumed to be a constant parameter in the whole operating frequency range of the motor. Impedance measurements also verified the value of C at frequencies much higher than the self-resonance, where the capacitive branch becomes dominant to the RLC branch of Fig. 1(b).

The series resistance R_s and reactance X_s are shown in Fig. 1(b). In terms of R_{ac} and L_{ac}, we have:

$$R_s = \frac{R_{ac}}{(1-\omega^2 L_{ac}C)^2 + (\omega C R_{ac})^2} \quad (39)$$

$$X_s = \frac{\omega L_{ac}(1-\omega^2 L_{ac}C) - (\frac{CR_{ac}^2}{L_{ac}})}{(1-\omega^2 L_{ac}C)^2 + (\omega C R_{ac})^2} \quad (40)$$

3. Results

In order to validate the effectiveness of the proposed model, an 8 kW counter-rotating PMSM, which is designed for submarine propulsion, is modeled by the proposed analytical method and compared with the 3D

FEA eddy-current analysis. Then, the high-frequency characteristic modeled for the one phase of the motor is compared with the measured motor impedance characteristic. Table I shows the motor specifications and design parameters. One phase of the motor is modeled based on the equivalent circuit of Fig. 1.

Fig. 4 shows the setup for impedance measurement of one phase of the 8kW counter-rotating PMSM measured with GW Instek LCR-8110G Precision LCR Meter. The motor is kept standstill with insulated bearings and also disconnected from other devices. The impedance is measured between the terminal of one phase and the neutral point of the star connection, as shown in Fig. 5.

TABLE I. 8KW PMSM MOTOR PROPERTIES

Description	Symbol	Value
Output Power (kW)	P_o	8
Rated Voltage (V)	V_o	220
Number of Pole pairs	P	4
Rated Speed (rpm)	ω_r	4000
Number of Stator Slots	Q	24
Outer Radius of Stator (mm)	R_{so}	69.75
Inner Radius of Stator (mm)	R_{si}	42.75
Length of Stator Core (mm)	l_s	100
Skew Width (number of slots)	S_{sp}	0.666667
Number of phases	m	3
Number of Parallel Branches	a	1
Number of Conductors per Slot	N_Q	60
Average Coil Pitch (number of slots)	y_Q	2
Wire Diameter (mm)	D_w	1.2
Wire Copper Diameter (mm)	D_c	1.1
Air Gap Length (mm)	δ	3.81
The thickness of Magnet (mm)	h_M	3
Width of Magnet (mm)	W_M	23.8183
Outer Radius of Rotor (mm)	R_{ro}	39.35
Inner Radius of Rotor (mm)	R_{ri}	29.34
Stator Slot Properties (mm)		
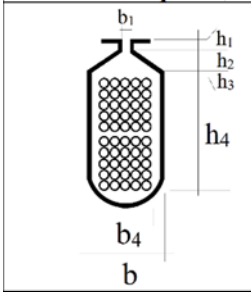	h_1	1.2
	h_2	0.4
	h_3	0.2
	h_4	12.27
	b_1	2
	b_4	7.54
	b	8.14

Fig. 4. Test 8kw PMSM impedance measurement setup

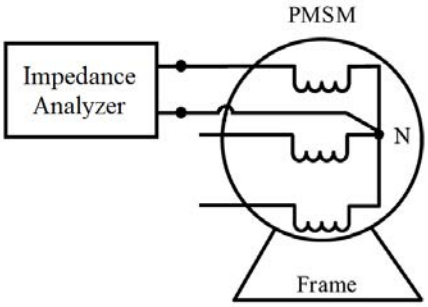

Fig. 5. Impedance measurement of one phase of the PMSM

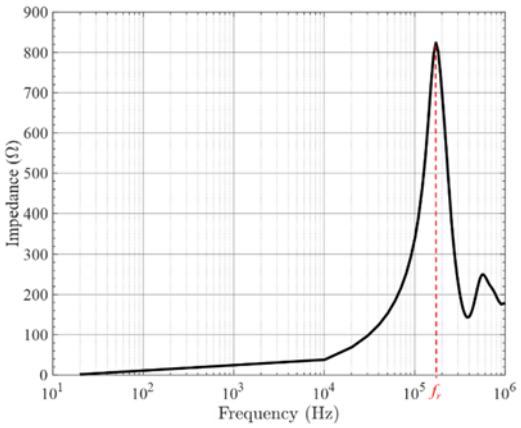

Fig. 6. Impedance characteristic of one phase of the PMSM Motor measured with GW Instek LCR-8110G Precision LCR Meter

Fig. 6 shows the impedance characteristic of one phase of the 8kW counter-rotating PMSM measured with GW Instek LCR-8110G Precision LCR Meter. Using the proposed method in previous sections, we can model this frequency behavior with a lumped parameters circuit shown in Fig. 1. The self-resonance frequency of the motor f_r=171.7 kHz is marked in Fig. 6. In order to represent the self-resonance point accurately, in addition to the R_{ac} and L_{ac} calculated from (37) and (38), the total capacitance of the winding should be estimated from (36), as it is explained in section II-C.

3D FEA simulation for the same geometry of one lamination of the core is executed in ANSYS Maxwell 3D using the eddy-currents solver. 3D FEA eddy-current analysis gives highly detailed results considering the high-frequency eddy-current effects, skin, and proximity effects in the simulations, which makes it an excellent criterion for verifying the analytical calculation results. Fig. 7 shows the geometry and meshing of the Maxwell 3D FEA simulation. For getting accurate results in FEA simulation, high numbers of meshing in the core and conductors are considered. The meshing operation of the iron-core must be done with the consideration of the highest frequency of the simulation. The Adaptive Frequency feature of the eddy-current solver in ANSYS Maxwell defines the frequency that the mesh

is constructed and adapted, and at which solution is obtained.

Higher frequency of the simulation calculations leads to high meshes in the edges and corners of stator slots and teeth, which means the requirement of significantly higher computational power and simulation time in comparison with the proposed analytical modeling solution.

Iron-core equivalent inductance $L_{m(ac)}$, and core loss equivalent resistance R_c is calculated in several frequencies from 100 Hz to 10 MHz using ANSYS Maxwell 3D. The eddy-current solver computes steady-state, time-varying (AC) magnetic fields at a given frequency for the assigned geometry. 3D eddy current solver is a full-wave solver and solves for displacement currents in the core. Conductors of one phase are excited as the source of the AC magnetic field by sinusoidal AC at different frequencies.
Fig. 8 shows the total AC resistance R_{ac} calculated from (37) for the considered geometry model of Fig. 7 compared to the 3D FEA simulation result. As can be seen with the increase of the frequency due to skin effect and proximity effect in the winding conductors, the value of the stator winding resistance R_w increases, also the core-loss equivalent resistance in the core R_c is increasing with the frequency. Thus, the total AC resistance R_{ac} value increases with the frequency. Both the analytical method and 3D FEA simulation results are in good agreement, which shows the effectiveness of the proposed analytical model. However, as it is stated before, 3D FEA requires significantly higher computational power and time compared to the analytical solution.

Fig. 9 shows the total AC inductance L_{ac} calculated from (38) for the geometry model in comparison with the 3D FEA simulation result. As it is expected because of eddy-currents in the core, which acts as a barrier for the magnetic flux magnetization inductance $L_{m(ac)}$ is decreasing with the increase of the frequency, also leakage inductance $L_{l(ac)}$ value decrease with frequency, thus the total AC inductance L_{ac} is decreasing with the increase of the frequency. A small deviation can be seen between the curves of L_{ac} calculated from the proposed model and 3D FEA. This deviation is mainly due to the calculation of leakage inductances. In 3D FEA, the exact geometry of the slots and teeth shapes are used to calculate the leakage inductances, but in analytical method leakage inductances are calculated based on equations derived from the simplified model of the motor slots and teeth shapes, so the results are not as accurate as 3D FEA solution.

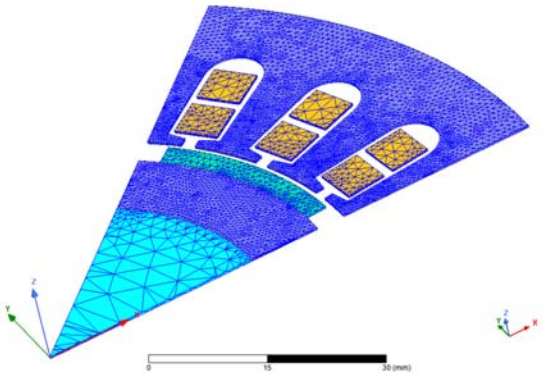

Fig. 7. The meshing of the simulation geometry of the PMSM motor in ANSYS Maxwell 3D

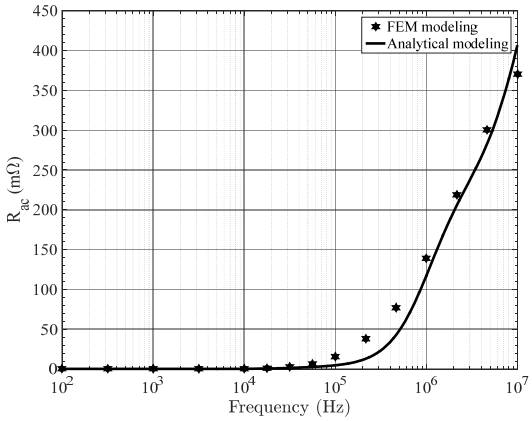

Fig. 8. Total AC resistance R_{ac} of the motor calculated from (37) in comparison with the 3D FEA simulation result.

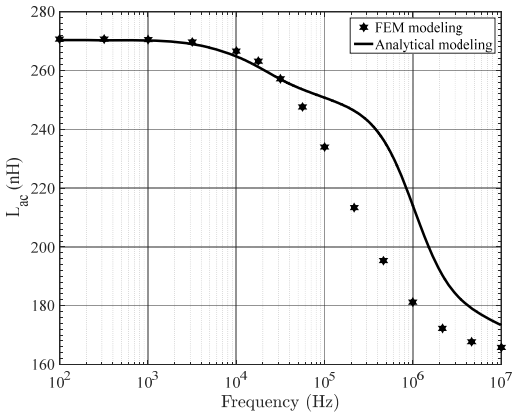

Fig. 9. Total AC Inductance L_{ac} of the motor calculated from (38) in comparison with the 3D FEA simulation result.

Now, the total parasitic capacitance C of the motor winding (see Fig.1a) can be calculated from substituting values of R_{ac}, L_{ac} at the resonance frequency f_r in (36). It should be noticed that the values in Figs. 8 and 9 are calculated for the geometry of Fig. 7. In order to calculate the phase values, they should be

multiplied by the number of poles p and the number of laminations n.

The total parasitic capacitance of each phase C calculated by (36) is equal to 2.73 nF. Now all the lumped parameters of the circuit model proposed in Fig. 1a is determined. Furthermore, Fig. 10 and Fig 11 show the equivalent series resistance and reactance of Fig. 1(b) calculated from (39) and (40). The effect of the parasitic capacitance in both equivalent series resistance R_s and reactance X_s can be seen. Now, we can calculate the phase impedance $Z_{ph}= R_s+jX_s$.

Fig. 12 shows the calculated impedance characteristic of one phase of the PMSM compared to the measurement data. It can be seen that low-frequency behavior is modeled reasonably accurately. The self-resonance point is an essential part of the modeling because usually, high-frequency motor models fail to represent this point correctly [4, 7, 9, 21]. Here, it can be seen that the proposed model successfully represents the self-resonance point of motor impedance with high accuracy. Because, in the proposed physics-based method, the actual geometry and physical properties of the materials of the motor are used to estimate the parasitic parameters of the circuit model.

At higher frequencies (over 200 kHz), there are corner frequencies in measured impedance characteristics, which are not captured in the proposed physics-based model (see Fig. 12). These corner frequencies are due to different high-frequency inter-turn effects of stator windings and need a more complex circuit model to describe the impedance [9, 11]. Additional circuit parameters can be added to the proposed model to represent these corner frequencies in PMSM impedance characteristics at higher frequencies.

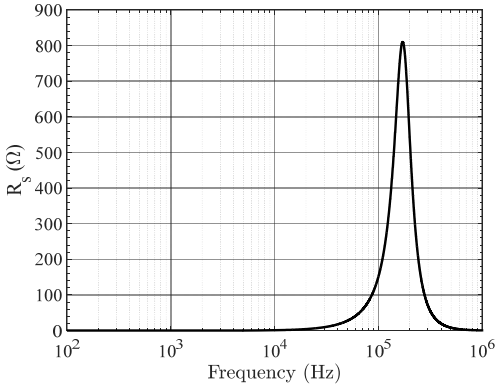

Fig. 10. Equivalent series resistance R_s, calculated by (39).

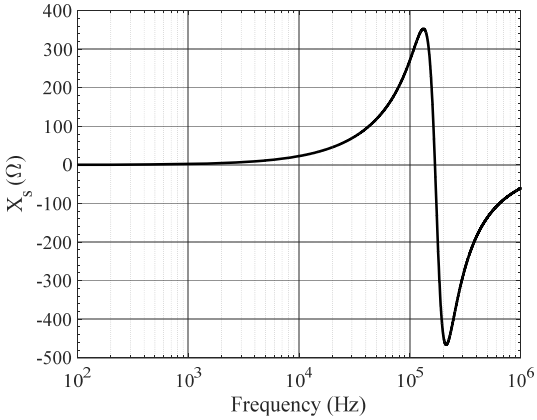

Fig. 11. Equivalent series reactance X_s calculated by (40).

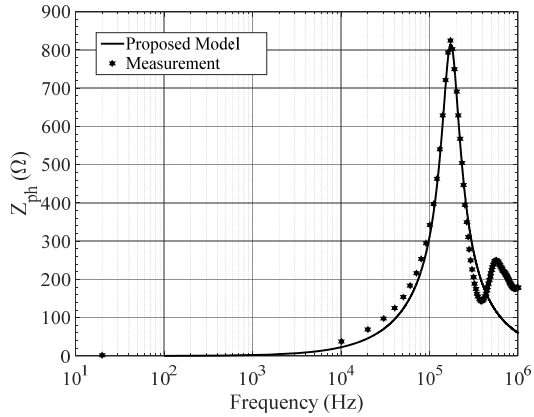

Fig. 12. Calculated impedance characteristics of one phase of the PMSM motor in comparison with measurement.

4. Conclusion

In this paper, a novel physics-based analytical modeling method is proposed to represent the high-frequency behavior of laminated iron-core PMSM. The hysteresis losses in the core are neglected. The total AC resistance and total inductance are frequency-dependent parameters because of the skin and proximity effects in the winding and the eddy-currents in the laminated iron-core. The total parasitic capacitance, which models the turn-to-turn and turn-to-iron core parasitic capacitances, is calculated from the first self-resonant frequency of the coil and is assumed to be frequency independent. The calculated results are in good agreement with the measurements carried out for the PMSM. Because the rotor can be neglected in high-frequency modeling of the motor [14], the proposed method can be used for modeling various kinds of AC motors with laminated iron-cores. The proposed model can be used for computer-aided simulations of laminated iron-core AC motors with an inverter drive system.

5. References

[1] E. Zhong and T. A. Lipo, "Improvements in EMC performance of inverter-fed motor drives," IEEE Transactions on Industry Applications, vol. 31, no. 6, pp. 1247-1256, 1995.

[2] G. L. Skibinski, R. J. Kerkman, and D. Schlegel, "EMI emissions of modern PWM AC drives," IEEE Industry Applications Magazine, vol. 5, no. 6, pp. 47-80, 1999.

[3] G. Grandi, D. Casadei, and U. Reggiani, "Equivalent circuit of mush wound AC windings for high frequency analysis," in ISIE'97 Proceeding of the IEEE International Symposium on Industrial Electronics, 1997, vol. 1, pp. SS201-SS206 vol. 1: IEEE.

[4] G. Grandi, D. Casadei, and A. Massarini, "High frequency lumped parameter model for AC motor windings," in European Conference on Power Electronics and Applications, 1997, vol. 2, pp. 2.578-2.583.

[5] A. Rahimi and K. Kanzi, "CM and DM Conducted EMI Modelling of PMSM VSD System with Non-ideal LISN," IET Electric Power Applications, 2020.

[6] R. Yang, B. Zhang, D. Qiu, and Z. Liu, "Time–frequency and wavelet transforms of EMI dynamic spectrum in chaotic converter," Power Electronics, IEEE Transactions on, vol. 24, no. 4, pp. 1083-1092, 2009.

[7] B. Mirafzal, G. L. Skibinski, R. M. Tallam, D. W. Schlegel, and R. Lukaszewski, "Universal induction motor model with low-to-high frequency-response characteristics," Industry Applications, IEEE Transactions on, vol. 43, no. 5, pp. 1233-1246, 2007.

[8] B. Mirafzal, G. L. Skibinski, and R. M. Tallam, "Determination of parameters in the universal induction motor model," Industry Applications, IEEE Transactions on, vol. 45, no. 1, pp. 142-151, 2009.

[9] M. Gries and B. Mirafzal, "Permanent magnet motor-drive frequency response characterization for transient phenomena and conducted EMI analysis," in Applied Power Electronics Conference and Exposition, 2008. APEC 2008. Twenty-Third Annual IEEE, 2008, pp. 1767-1775: IEEE.

[10] C. Bi et al., "High-frequency electric-motor modelling for conducted CM current prediction in adjustable speed drive system," IET Power Electronics, vol. 11, no. 7, pp. 1257-1265, 2018.

[11] Y. Wu et al., "High-frequency modelling of permanent magnet synchronous motor with star connection," Electric Power Applications, vol. 12, no. 4, pp. 539-546, 2018.

[12] A. F. Moreira, T. A. Lipo, G. Venkataramanan, and S. Bernet, "High frequency modeling for cable and induction motor overvoltage studies in long cable drives," in Industry Applications Conference, 2001. Thirty-Sixth IAS Annual Meeting. Conference Record of the 2001 IEEE, 2001, vol. 3, pp. 1787-1794: IEEE.

[13] I. Stevanovic, B. Wunsch, G. Madonna, M. Vancu, and S. Skibin, "Multiconductor cable modeling for EMI simulations in power electronics," in IECON 2012 - 38th Annual Conference on IEEE Industrial Electronics Society, 2012, pp. 5382-5387.

[14] B. Mirafzal, G. L. Skibinski, R. M. Tallam, D. W. Schlegel, and R. Lukaszewski, "Universal induction motor model with low-to-high frequency-response characteristics," IEEE Transactions on Industry Applications, vol. 43, no. 5, pp. 1233-1246, 2007.

[15] J. Luszcz, High Frequency Conducted Emission in AC Motor Drives Fed By Frequency Converters: Sources and Propagation Paths. John Wiley & Sons, 2018.

[16] K. Maki, H. Funato, and L. Shao, "Motor modeling for EMC simulation by 3-D electromagnetic field analysis," in Electric Machines and Drives Conference, 2009. IEMDC'09. IEEE International, 2009, pp. 103-108: IEEE.

[17] O. Mohammed and S. Ganu, "FE-circuit coupled model of electric machines for simulation and evaluation of EMI issues in motor drives," Magnetics, IEEE Transactions on, vol. 46, no. 8, pp. 3389-3392, 2010.

[18] A. Sarikhani, A. Nejadpak, and O. Mohammed, "Coupled field-circuit estimation of operational inductance in PM synchronous machines by a real-time physics-based inductance observer," IEEE transactions on magnetics, vol. 49, no. 5, pp. 2283-2286, 2013.

[19] A. Nejadpak and O. A. J. I. t. o. m. Mohammed, "Physics-based modeling of power converters from finite element electromagnetic field computations," vol. 49, no. 1, pp. 567-576, 2012.

[20] M. Barzegaran, A. Mohamed, T. Youssef, and O. A. J. I. t. o. m. Mohammed, "Electromagnetic signature study of a power converter connected to an electric motor drive," vol. 50, no. 2, pp. 201-204, 2014.

[21] G. Vidmar and D. Miljavec, "A Universal High-Frequency Three-Phase Electric-Motor Model Suitable for the Delta- and Star-Winding Connections," IEEE Transactions on Power Electronics, vol. 30, no. 8, pp. 4365-4376, 2015.

[22] M. A. Lotfi motlagh and K. Kanzi, "Measurement, Modeling and Evaluation of Differential-mode Impedance in an ESP Motor," presented at the 33th Power System Conference (PSC 2018), Tehran, Iran, 22-24 Oct, 2018.

[23] G. Grandi, M. K. Kazimierczuk, A. Massarini, U. Reggiani, and G. Sancineto, "Model of laminated iron-core inductors for high frequencies," IEEE Transactions on magnetics, vol. 40, no. 4, pp. 1839-1845, 2004.

[24] J. Pyrhonen, T. Jokinen, and V. Hrabovcova, Design of rotating electrical machines. John Wiley & Sons, 2013.